UC Berkeley
UC Berkeley Previously Published Works

Title
Structure and Ionic Conductivity of Polystyrene-block-poly(ethylene oxide) Electrolytes in the High Salt Concentration Limit

Permalink
https://escholarship.org/uc/item/4m53s1n2

Authors
Chintapalli, M
Le, TNP
Venkatesan, NR
et al.

Peer reviewed

Structure and Ionic Conductivity of Polystyrene-*block*-poly(ethylene oxide) Electrolytes in the High Salt Concentration Limit

Mahati Chintapalli,[†,⊥] Thao N. P. Le,[‡] Naveen R. Venkatesan,[†,‡] Nikolaus G. Mackay,[‡] Adriana A. Rojas,[‡,§] Jacob L. Thelen,[‡,§,⊥] X. Chelsea Chen,[⊥] Didier Devaux,[§,∥] and Nitash P. Balsara*,[‡,§,∥,⊥]

[†]Department of Materials Science and Engineering and [‡]Department of Chemical and Biomolecular Engineering, University of California, Berkeley, Berkeley, California 94720, United States

[§]Joint Center for Energy Storage Research (JCESR), [∥]Environmental Energy Technologies Division, and [⊥]Materials Sciences Division, Lawrence Berkeley National Laboratory, Berkeley, California 94720, United States

Ⓢ *Supporting Information*

ABSTRACT: We explore the relationship between the morphology and ionic conductivity of block copolymer electrolytes over a wide range of salt concentrations for the system polystyrene-*block*-poly(ethylene oxide) (PS-*b*-PEO, SEO) mixed with lithium bis-(trifluoromethanesulfonyl)imide salt (LiTFSI). Two SEO polymers were studied, SEO(16−16) and SEO(4.9−5.5), over the salt concentration range $r = 0.03−0.55$. The numbers x and y in SEO($x−y$) are the molecular weights of the blocks in kg mol^{-1}, and the r value is the molar ratio of salt to ethylene oxide moieties. Small-angle X-ray scattering was used to characterize morphology and grain

size at 120 °C, differential scanning calorimetry was used to study the crystallinity and the glass transition temperature of the PEO-rich microphase, and ac impedance spectroscopy was used to measure ionic conductivity as a function of temperature. The most surprising observation of our study is that ionic conductivity in the concentration regime $0.11 \leq r \leq 0.21$ increases in SEO electrolytes but decreases in PEO electrolytes. The maximum in ionic conductivity with salt concentration occurs at about twice the salt concentration in SEO ($r = 0.21$) as in PEO ($r = 0.11$). We propose that these observations are due to the effect of salt concentration on the grain structure in SEO electrolytes.
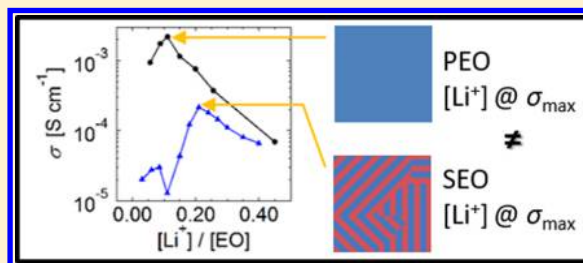
INTRODUCTION

Solid polymer electrolytes have several advantages over traditional organic liquid electrolytes in lithium batteries including low flammability, high electrochemical stability, and mechanical stiffness.[1−6] A subset of solid polymer electrolytes, block copolymers mixed with lithium salts, are particularly interesting because they take advantage of microphase separation to decouple the materials responsible for ion transport and mechanical stiffness, two typically antagonistic properties.[7−12] In this study we consider the system polystyrene-*block*-poly(ethylene oxide) (SEO) mixed with lithium bis(trifluoromethanesulfonyl)imide (LiTFSI) salt. The polystyrene (PS) block provides mechanical stiffness, and the poly(ethylene oxide) (PEO) block solvates and transports ions derived from LiTFSI.[12−15]

Ion transport in block copolymers is determined both by the properties of the ion conducting block and by the nano- and mesoscale structure of the electrolyte.[12,15−22] The crystallinity and ion transport of PEO homopolymer mixed with LiTFSI, as well as with other salts, have been thoroughly investigated in the literature.[23−35] In PEO/LiTFSI mixtures, it is known that ionic conductivity reaches a maximum with salt concentration around an r value of 0.1, where r is the molar ratio of salt to

ethylene oxide (EO) moieties.[31] Ionic conductivity rapidly decreases at higher salt concentrations due to ion-pairing and transient cross-linking of the PEO chains.[26−30] Because of the low ionic conductivity of PEO/LiTFSI mixtures at high r values, with a few isolated exceptions, the high concentration regime has largely been ignored in studies on block copolymers such as SEO/LiTFSI.[14,15,36] Recently, Bates et al. studied mixtures of LiTFSI and PS and PEO chains grafted onto a polynorbornene backbone over the salt concentration range $0.05 \leq r \leq 0.5$ and showed that conductivity was maximized at a salt concentration of $r = 0.1$, similar to that in homopolymer PEO/LiTFSI mixtures.[37] However, Hudson showed that the maximum in conductivity in a particular SEO/LiTFSI mixture occurred at $r = 0.14$, significantly higher than the salt concentration that maximizes conductivity in PEO.[38] Thus, it is important to further investigate the behavior of SEO electrolytes at high salt concentrations. This study examines morphology, crystallinity, and ionic conductivity of SEO over a wide range of salt concentrations using small-angle X-ray

scattering (SAXS), differential scanning calorimetry (DSC), and ac impedance spectroscopy. In PEO, salt precipitation occurs at r values around 0.5.[31] In this study, we probe SEO/LiTFSI mixtures with salt concentrations over the entire solubility range, with r varying from 0.03 to 0.55.

■ EXPERIMENTAL SECTION

Electrolyte Preparation. The polymers used in this study, their number-averaged molecular weights, M_n, dispersity, Đ, and PEO volume fraction, ϕ_{PEO}, are given in Table 1.

Table 1. Characteristics of Polymers Used[a]

name	$M_{n,PS}$ (kg mol^{-1})	$M_{n,PEO}$ (kg mol^{-1})	Đ	ϕ_{PEO}
SEO(16−16)	16	16	1.09	0.49
SEO(4.9−5.5)	4.9	5.5	1.04	0.52
PEO(5)		5.0	1.06	1.0

[a]Number-averaged molecular weights, M_n, dispersity, Đ, and PEO volume fraction, ϕ_{PEO}, are given.

Block copolymers were synthesized by sequential anionic polymerization.[39,40] The PS block was synthesized first using a *sec*-butyllithium initiator. An aliquot was removed from the reaction to characterize the absolute molecular weight of the intermediate product using gel permeation chromatography (GPC; Viscotek GPCMax) in tetrahydrofuran (THF), with triple detection (viscometry, low angle light scattering, and refractive index detection). The PEO block was synthesized using P4 phosphazene base to promote and isopropyl alcohol to terminate the polymerization. The ratio of PEO to PS was determined by ^{1}H NMR (Bruker Avance 500), and the block copolymer dispersity was determined by GPC using *N,N*-dimethylformamide solvent and PS standards. SEO in benzene solution was passed through a neutral alumina column to remove trace P4 base and then lyophilized (Millrock LD85 lyophilizer) to produce a white powder.[41] Pure PEO (PEO(5), $M_n = 5$ kg mol^{-1}) was purchased from and characterized by PolymerSource, Inc. The ionic conductivity of PEO(5) is similar to that of higher molecular weight PEO.[42,43]

Electrolytes of varying salt concentrations were prepared from the three polymers SEO(16−16), SEO(4.9−5.5), and PEO(5). LiTFSI was purchased from Novolyte. Because of the hygroscopic nature of LiTFSI, electrolyte materials were dried and handled in an argon glovebox with the H$_2$O level maintained below 0.1 ppm. Polymers were dried under vacuum at 90 °C for 24 h, and LiTFSI was dried at 120 °C for 72 h before being brought into the glovebox by air-free transfer. LiTFSI was dissolved in anhydrous THF and added to solutions of SEO in anhydrous benzene. For ease of lyophilization, the concentration of the LiTFSI−THF stock solution was adjusted so that the final solutions contained less than 5 vol % THF. Solutions were lyophilized without exposure to air for 1 week. Fifteen salt concentrations were prepared for each SEO polymer spanning the range $r = 0.03$ to $r = 0.55$. PEO solutions were prepared by dissolving both the polymer and salt in tetrahydrofuran and evaporating on a hot plate at 45 °C for 72 h. Eight concentrations were prepared between $r = 0.06$ and $r = 0.55$. Both PEO and SEO solutions were dried under vacuum at 90 °C for 24 h to remove trace solvents. In all samples, solvent and water content was below the detection limit of ^{1}H NMR.

Sample Preparation. Samples for conductivity measurements were prepared by heat-pressing the polymer at 130 °C into a 150 μm thick fiberglass−epoxy annular spacer (Garolite-10). The diameter of the electrolyte was taken to be the size of the hole in the annulus, 3.175 mm. High-purity aluminum foils, 17.5 μm thick, were pressed onto either side of the polymer as electrodes, and aluminum tabs (MTI corporation) were attached to the electrodes with polyimide tape. The sample assembly was vacuum-sealed in an airtight aluminum-reinforced polypropylene pouch (Showa Denka) with tabs protruding out so the sample could be electrically probed. The thickness of the polymer sample was measured after conductivity measurements were performed using a precision micrometer.

Samples for SAXS measurements were made using a similar method to those prepared for conductivity measurements. No tabs or aluminum electrodes were attached. Polyimide film 25 μm thick was heat-pressed to either side of the sample at 130 °C to prevent electrolyte from flowing out of the spacer when heated. The samples were vacuum-sealed in a modified airtight pouch. To improve X-ray transmission through the pouch, holes were punched through the material, and 25 μm polyimide windows were glued over the holes using a low vapor pressure epoxy sealant. The modified pouches were dried at 120 °C for 24 h prior to use to remove trace solvents from the sealant. A blank sample for subtraction of the scattering background was produced in a similar manner to the other samples but without electrolyte.

Small-Angle X-ray Scattering. SAXS measurements were performed at beamline 7.3.3 at the Advanced Light Source synchrotron (Berkeley, CA).[44] Samples were annealed for 24 h at 130 °C prior to measurement and were measured at 120 °C, above the glass transition temperatures of all of the constituents of the samples. Scattering was performed using 10 keV X-rays, and transmission was monitored using pre- and postsample ion chambers. Two-dimensional diffraction images were captured with a Dektris Pilatus 2M camera with a pixel size of 0.172 × 0.172 mm, and images were calibrated using a silver behenate standard. The distance between the sample and detector was 3.8 m, and the exposure time was 10 s. Two-dimensional images were azimuthally integrated to produce one-dimensional scattering profiles using the Nika package in Igor Pro.[45] Scattering of the pouch material was subtracted according to eq 1:

$$I_{Corrected} = I_{Sample} - \frac{T_{Sample}}{T_{Blank}} I_{Blank} \tag{1}$$

where $I_{Corrected}$ is the corrected scattering intensity, I_{Sample} is the scattering profile from the sample, T_{Sample} is the transmission of the sample, I_{Blank} is the scattering from the blank, and T_{Blank} is the transmission of the blank.

AC Impedance Spectroscopy. Ionic conductivity was measured using ac impedance spectroscopy, and sample temperature was controlled using a home-built heat stage. Prior to making conductivity measurements, samples were annealed at 130 °C for 3 h. After annealing, the conductivities of the samples were invariant over the period of an hour. For SEO electrolytes, temperature-dependent conductivity measurements were taken at 10 °C increments as the samples were cooled from 130 to 30 °C. For PEO electrolytes, measurements were taken at 5−10 °C increments as the samples were cooled from 90 to 25 °C. The samples were held at constant temperature for 1 h prior to each measurement. Ac impedance measurements were performed using a potentiostat (BioLogic VMP3), and the amplitude of the probe signal was 20 mV, while the frequency was varied from 1 MHz to 1 Hz. An example Nyquist plot is given in Figure S1 of the Supporting Information. The minimum in the Nyquist plot of impedance was taken as the bulk resistance of the electrolyte, R. The spacer area, a, and the measured sample thickness, t, were used to calculate the conductivity according to eq 2.

$$\sigma = \frac{t}{Ra} \tag{2}$$

Differential Scanning Calorimetry. Thermal transitions were measured using DSC (TA Instruments Q2000). Samples were hermetically sealed in aluminum pans in an argon glovebox. Samples were heated at 10 °C min^{-1} from 40 to 130 °C (first heating), quickly equilibrated to −80 °C, and then heated at 10 °C min^{-1} from −80 to 130 °C (second heating). The glass transitions temperatures of PEO and PS, $T_{g,PEO}$ and $T_{g,PS}$, and the melting temperature of nearly pure PEO, $T_{m,PEO}$, are reported from the second heating. Melting peaks of intermediate PEO compounds are reported from the first heating as they were not observed in the second heating.

Transmission Electron Microscopy. Selected samples of SEO(16−16) were imaged using scanning transmission electron microscopy (STEM) after annealing at 130 °C for 24 h, the same heat treatment used for preparing SAXS samples.[17] Samples were cryo-
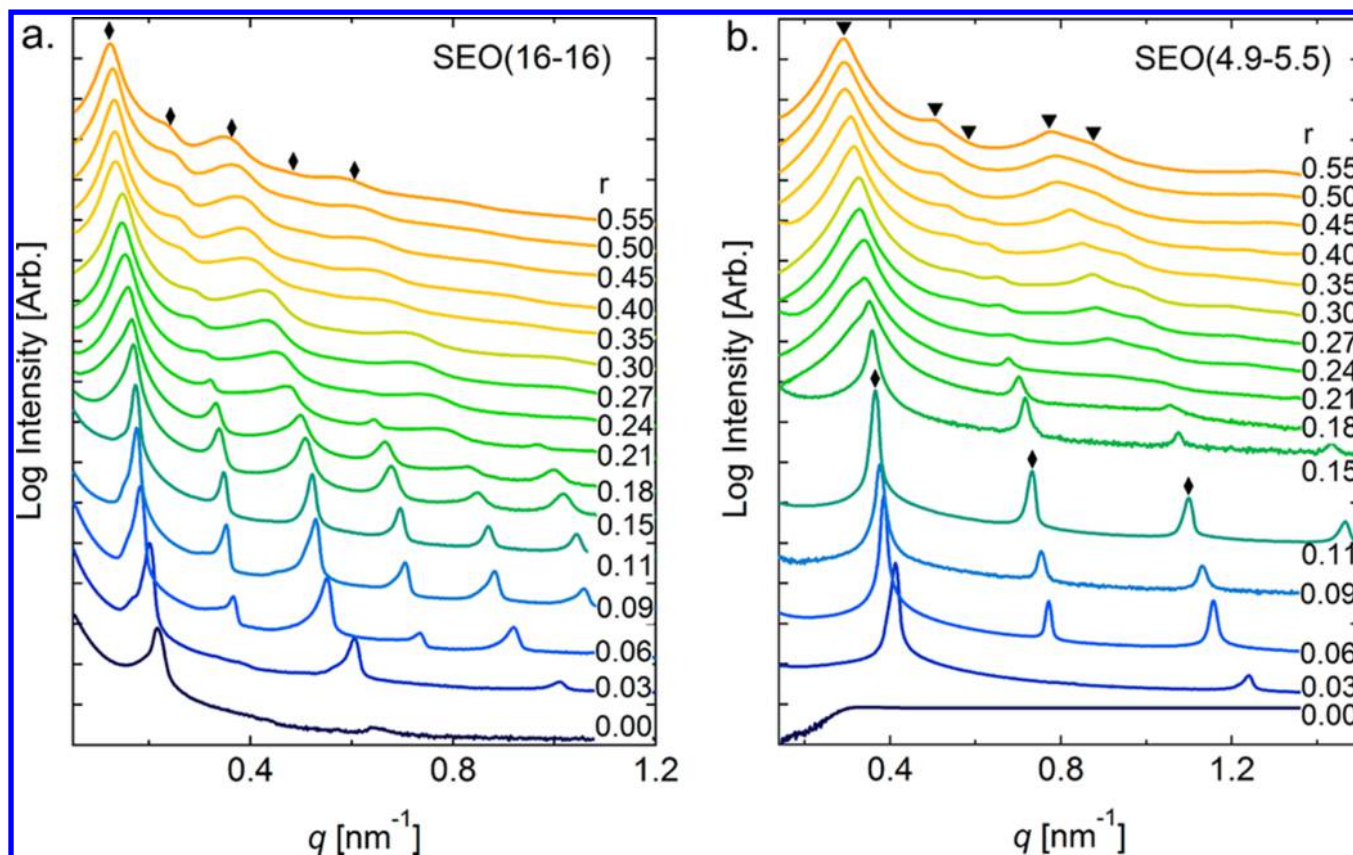
Figure 1. Small-angle X-ray scattering profiles of SEO electrolytes at 120 °C. Scattering intensity is plotted as a function of the magnitude of the scattering vector q. In (a) profiles are shown for SEO(16−16), and in (b) profiles are shown for SEO(4.9−5.5). The salt concentration of each profile is indicated on the right. Profiles are shifted vertically. Diamonds indicate peaks due to lamellar order (q^*, $2q^*$, $3q^*$, $4q^*$, $5q^*$), and triangles indicate peaks due to cylindrical order (q^*, $\sqrt{3}q^*$, $2q^*$, $\sqrt{7}q^*$, $3q^*$).

microtomed (Leica FC6) to an approximate thickness of 100 nm, stained with RuO_4 for 10 min, and transferred to a lacey carbon-coated copper grid. Dark field images were obtained on a Tecnai F20 UT FEG instrument using a high angle annular dark field detector (HAADF) and 200 keV acceleration voltage. Bright regions are PEO.[46] Samples were briefly exposed to air during microtoming and transfer to the microscope.

RESULTS AND DISCUSSION

In Figure 1, SAXS profiles taken at 120 °C are shown for SEO electrolytes. The intensity is plotted as a function of scattering vector, q, where $q = 4\pi \sin \theta/\lambda$, 2θ is the scattering angle, and λ is the wavelength of the X-rays. Data for SEO(16−16) are shown in Figure 1a. At all salt concentrations, SEO(16−16) exhibits lamellar morphology. All of the scattering profiles contain a primary scattering peak at $q = q^*$ and higher order scattering peaks that index to a lamellar morphology. At $r =$ 0.06 and above, higher order peaks at $2q^*$, $3q^*$, $4q^*$, etc., are seen. The expected locations of the higher order peaks for the r = 0.55 sample are indicated by arrows in Figure 1a. At $r = 0.03$ and 0.00, the even order peaks are suppressed, indicating a nearly symmetric lamellar structure. Even order peaks are also suppressed at high salt concentrations. SAXS data for SEO(4.9−5.5) are shown in Figure 1b. The neat SEO(4.9−5.5) ($r = 0$) is disordered. The decrease in scattering intensity at low q for neat SEO(4.9−5.5) is an artifact due to slight errors in background subtraction. The SAXS patterns of SEO(4.9−5.5) electrolytes at low salt concentrations ($0.03 \leq r \leq 0.11$) are similar to those of SEO(16−16); the expected locations of

the $2q^*$ and $3q^*$ peaks in the $r = 0.11$ sample are shown in Figure 1b. We conclude that these samples have a lamellar morphology. The SAXS patterns at high concentrations ($r \geq$ 0.24) are qualitatively different. At the highest salt concentration studied ($r = 0.55$), higher order peaks at $\sqrt{3}q^*$, $2q^*$, $\sqrt{7}q^*$, etc., are seen; the arrows near the $r = 0.55$ SAXS pattern in Figure 1b indicate the expected locations of higher-order peaks corresponding to hexagonally packed cylinders. We conclude that this sample contains PS cylinders in a PEO/ LiTFSI matrix. The SAXS patterns of samples with the range $0.27 \leq r \leq 0.55$ are qualitatively similar, indicating the presence of hexagonally packed PS cylinders. In the salt concentration range $0.18 \leq r \leq 0.24$, SAXS signatures of both lamellar and cylindrical phases are present. This is most clearly seen in the r = 0.18 sample (Figure 1b), where the q^* peak appears to be composed of two overlapping Gaussian peaks. We conclude that lamellar and cylindrical phases coexist in the range $0.18 \leq r$ ≤ 0.24. The data in Figure 1b are consistent with those reported in ref 47. It was shown in ref 47 that pure SEO(4.9− 5.5) has an order−disorder transition near room temperature;[47] hence, no microphase separation is observed at 120 °C. Morphological changes are seen in the weakly segregated electrolyte (SEO(4.9−5.5)). This is anticipated from well-established theories on microphase separation of neat block copolymers.[48,49] The difference in morphology behavior with salt concentration between the two polymers can be explained by the fact that in SEO(4.9−5.5) ϕ_{PEO} (Table 1) is greater and the number of statistical segments, N, is less than in SEO(16− 16). Both of these parameters make the lamellar−cylinder
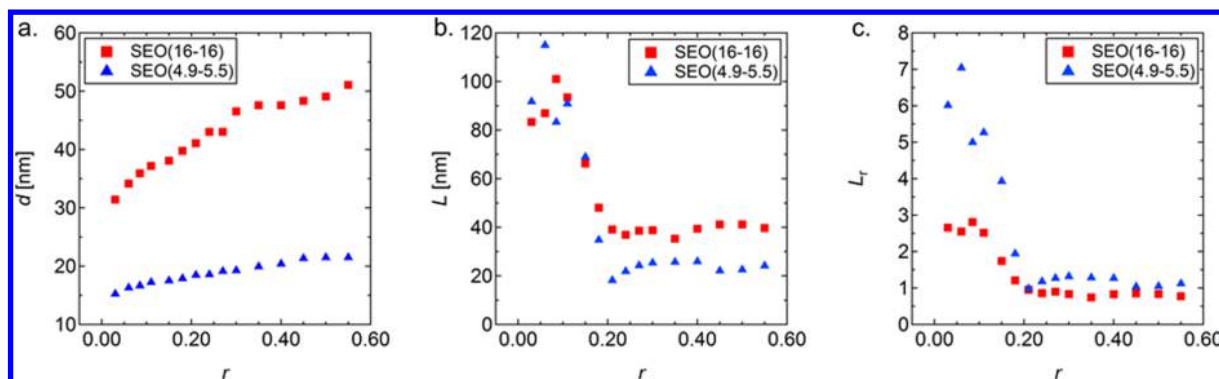
Figure 2. Domain spacing and grain size as a function of salt concentration for SEO(16−16) and SEO(4.9−5.5). In (a) domain spacing, d, is plotted as a function of salt concentration, r. In (b) and (c), grain size, L, and reduced grain size, L_r, are plotted versus salt concentration. The data in Figure 2 are based on SAXS profiles measured at 120 °C.

transition more accessible in SEO(4.9−5.5) than SEO(16−16).[50,51]

As salt concentration increases, both SEO(16−16) and SEO(4.9−5.5) show changes in the primary peak position, q^*, and full width at half-maximum, F. As salt concentration increases, q^* shifts to lower values, indicating swelling of the domains. The characteristic domain spacing, d, is given by the equation $d = 2\pi / q^*$ and is plotted against r in Figure 2a. The data in Figure 2 are derived from SAXS profiles obtained at 120 °C. For SEO(16−16), d increases from 31 nm at $r = 0.03$ to 51 nm at $r = 0.55$ (61% increase), and for SEO(4.9−5.5), d increases from 15 nm at $r = 0.03$ to 21 nm at $r = 0.55$ (70% increase). For both polymers d increases more or less smoothly over the entire range of r values despite the morphology change in the SEO(4.9−5.5) system.

In both polymers, F becomes larger with increasing salt concentration, indicating a decrease in grain size. F was measured by fitting a linear baseline in the vicinity of the primary peak and using linear interpolation between data points to find the width at half of the peak maximum.[17] Assuming that the primary contribution to peak broadening is finite grain size, according to the Scherrer equation, the average grain size, $L \approx 1/F$.[52] We neglect contributions of instrumental peak broadening and grain anisotropy[53,54] in estimating L. Lamellar and hexagonally packed cylinder morphologies are periodic in one and two dimensions, respectively. We note that for lamellae L corresponds to the average height of a lamellar stack, and for hexagonally packed cylinders, L corresponds to the average width of the grain in the radial plane of the cylinders.[55] Grain size is plotted as a function of r in Figure 2b. For both polymers, below $r = 0.11$, L is relatively large and scattered around 90 nm. Between $r = 0.11$ and $r = 0.21$, grain size decreases, and above $r = 0.21$, the value of L reaches a minimum plateau. From the average and standard deviation of the data for L above $r = 0.21$, the plateau value is 39 ± 2 nm for SEO(16−16) and 24 ± 2 nm for SEO(4.9−5.5). These minimum values of grain size are close to the values of domain spacing for each polymer, indicating a high degree of disorder at high salt concentrations. In theory, the smallest possible grain size is on the order of one domain; hence, the lower limit of grain size has been reached.[56,57] It is thus instructive to examine the dependence of reduced grain size defined as $L_r = L/d$ on salt concentration. The reduced grain size represents the average number of repeated structures (lamellae or cylinders) in a grain. In Figure 2c, we plot L_r versus r. Unlike L, L_r does not depend on the polymer domain spacing or

molecular weight. Figure 2c shows that for $r \geq 0.21$ the reduced grain size reaches unity for both polymers. At salt concentrations below 0.21, on average, SEO(4.9−5.5) electrolytes contain more lamellae per grain than SEO(16−16) electrolytes do.

Transmission electron microscopy (TEM) was used to confirm our conclusions regarding the morphology of the electrolytes. Micrographs obtained from SEO(16−16) at selected salt concentrations are shown in Figure 3. A reduction
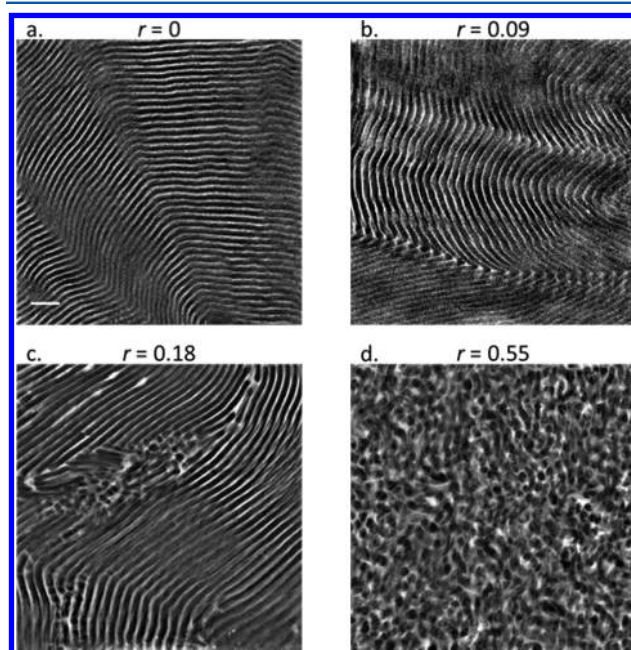

Figure 3. Dark field STEM images of SEO(16−16) at several salt concentrations. Salt concentration increases from (a) through (d). Polymers were stained with RuO_4, and PEO domains appear bright. The scale bar in (a) represents 100 nm, and it applies to all images.

in grain size with increasing salt concentration is clearly seen in Figure 3. In small regions of the image in Figure 3c, evidence of perforated lamellae is observed. Because we do not observe clear signatures of perforated lamellar morphology in the SAXS profiles in Figure 1a, all lamellae are treated as non-perforated in the subsequent analysis. In Figure 3d, the lack of long-range order at $r = 0.55$ suggests that our assignment of $L = 39$ nm $\approx d$ is correct.

In fully ordered block copolymers, grain growth occurs via defect annihilation.[58,59] Defects such as grain boundaries are metastable and will be annihilated given sufficient time and thermal activation.[59,60] As the samples were all annealed at the same temperature (130 °C) and for the same amount of time (24 h) prior to SAXS measurements, the fact that grain size is smaller at larger salt concentrations is an indication that annealing kinetics are slower at these concentrations. In lamellar and hexagonally packed cylinder systems, grain boundary morphology has been extensively characterized.[61−64] Ryu et al. proposed that grain growth kinetics in lamellar block copolymers are influenced by the types of grain boundaries present in a sample, as some structures such as low angle tilt boundaries have a low energetic barrier to annihilation, whereas other structures such as twist boundaries have a high barrier to annihilation.[59,60,65] Low energy barrier defects can be annihilated without requiring the polymer chains to diffuse across incompatible domains, while high barrier defects are annihilated either by long-range collective diffusion of polymer chains or diffusion of chains across incompatible domains.[59,60] Similar principles have been found to apply to the annealing of hexagonally packed cylinder thin films.[66−68] Diffusion of block copolymer chains in the direction perpendicular to the lamellar plane decreases as an exponential function of χN, where χ is the Flory−Huggins interaction parameter and N is the number of statistical segments.[69−71] Dissolving salt selectively in one of the blocks of a block copolymer increases the effective incompatibility between blocks. While the effective χ increases linearly with salt concentration in the low concentration limit,[19,36,47,72−74] more complex behavior is obtained at high salt concentrations.[47] In addition to thermodynamic effects, slowing down of segmental motion due to interactions between the PEO block and salt may also influence grain growth.[26−31] It follows that grain growth and defect annihilation would be slower in block copolymers containing higher salt concentration.

In addition to influencing the block copolymer morphology, salt concentration influences microscopic structure and dynamics of the PEO domains. The homopolymer PEO/LiTFSI system has been the subject of numerous studies.[28−35] Several salt concentration-dependent effects have been documented such as suppression or inhibition of PEO crystallinity, shifting of the PEO glass transition temperature ($T_{g,PEO}$) and melting point (T_m), formation of intermediate crystalline compounds, and changes in crystallization kinetics.[29−32] We explore the impact of salt concentration on the PEO block of SEO. To explore the effect of salt concentration on PEO, $T_{g,PEO}$ and $T_{m,PEO}$ were measured using DSC for PEO(5), SEO(4.9−5.5), and SEO(16−16) (second heating data). For the block copolymers, $T_{g,PS}$ was also measured and was nearly invariant with salt concentration. Between r = 0.06 and 0.15, the $T_{g,PS}$ for SEO(4.9−5.5) increased from 73.9 to 81.9 °C. The average value of $T_{g,PS}$ for SEO(4.9−5.5) above r = 0.15 was 82.1 ± 0.2 °C, and the average value for SEO(16−16) at all concentrations was 95.0 ± 0.1 °C. Unlike $T_{g,PS}$, $T_{g,PEO}$ varies significantly with salt concentration for all three polymers. The $T_{g,PEO}$ for PEO(5), SEO(16−16), and SEO(4.9−5.5) are shown as a function of salt concentration in Figure 4. As SEO(16−16) is highly crystalline below r = 0.09, reliable $T_{g,PEO}$ values could not be obtained in that concentration regime. Below r = 0.27, the values of $T_{g,PEO}$ for all three polymers coincide. Above r = 0.27, the values of $T_{g,PEO}$ are only similar for the block copolymers.
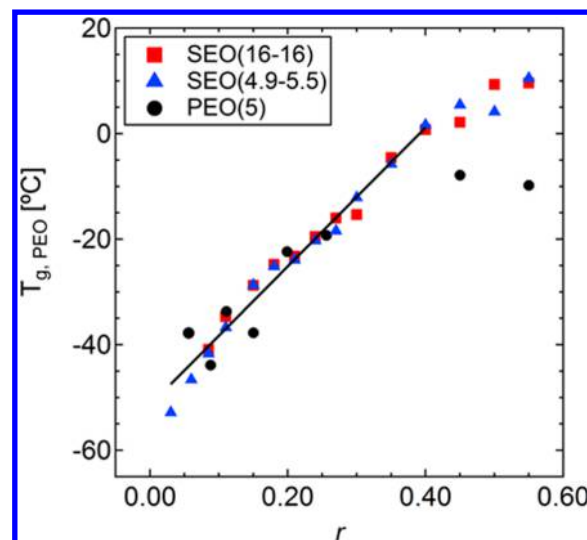

Figure 4. Glass transition temperature of PEO-rich microphases and PEO homopolymer, $T_{g,PEO}$, as a function of salt concentration, r. The line represents a least-squares fit through the data, for $0.03 \leq r \leq 0.40$. The line is given by $T_{g,PEO} = -51.4 + 131 \, r$ [°C].

At high salt concentrations (r = 0.45 and 0.55), $T_{g,PEO}$ for homopolymer PEO reaches a plateau. Our result is similar to that of Lascaud et al., who showed that for salt concentrations above r = 0.4, pure LiTFSI precipitation occurs, and $T_{g,PEO}$ saturates.[31] At the highest salt concentration, r = 0.55, we found evidence of macrophase separation in PEO(5)/LiTFSI mixtures using the naked eye. For the block copolymers, $T_{g,PEO}$ increases over the entire concentration range, which is evidence that after initial heating to 130 °C LiTFSI remains dissolved over the time scale of the DSC scan (30 min).

It appears that solubility of LiTFSI in SEO electrolytes is greater than that of PEO electrolytes; this may be due to thermodynamic or kinetic reasons. Microphase separation distorts the PEO chains, which may influence thermodynamic interactions between the polymer and salt. Precipitation kinetics could be slower in block copolymers due to confinement effects.[75,76] In a homogeneous polymer, dissolved ions can diffuse from any part of the volume to deposit on a growing precipitate nucleus, whereas in a block copolymer, ions can only diffuse to a nucleus within a continuous domain. Several studies have shown that in lamellar SEO, the PEO domain crystallizes in an oriented manner.[77−79] Oriented crystallization could occur in SEO/LiTFSI mixtures, which may slow the crystallization kinetics. Because of uncertainty about LiTFSI solubility at high salt concentrations, the conductivity data in this study are limited to $r \leq 0.40$, and the line in Figure 4 is fit to data for SEO and PEO electrolytes with $r \leq 0.40$. The line is given by $T_{g,PEO} = -51.4 + 131 \, r$ [°C].

The crystallization behavior of the PEO blocks in SEO(16−16) and SEO(4.9−5.5) was also measured by DSC. In Figures 5a and 5b, representative DSC heating scans are presented for SEO(16−16). Figure 5a shows second heating data. In Figure 5a, an endothermic peak at 55 °C is observed for the sample with r = 0.03, which we attribute to $T_{m,PEO}$, the melting of nearly pure PEO. Similar peaks were observed in samples with $r \leq 0.09$. At higher salt concentrations, a glass transition is observed at temperatures between −40 and 10 °C, reflecting the T_g of the salt-containing PEO-rich phase, $T_{g,PEO}$. The $T_{g,PEO}$ is also observed in all traces, though it is very weak in
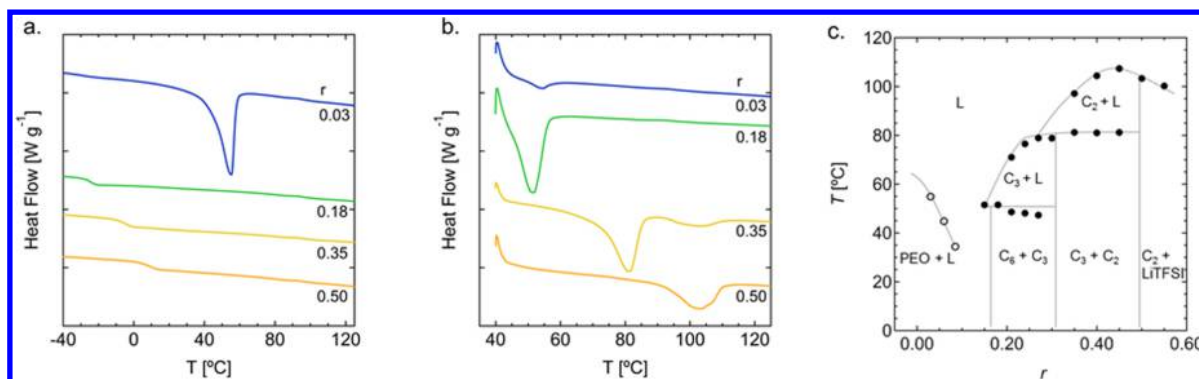
Figure 5. Differential scanning calorimetry and phase diagram of SEO(16−16)/LiTFSI electrolytes with different salt concentrations, r. In (a) and (b), thermograms obtained by differential scanning calorimetry are offset along the vertical axis, with endothermic peaks down. The ticks on the vertical axes are separated by 0.5 Wg^{-1}. In (a) thermograms from the second heating are shown, and in (b), thermograms from the first heating are shown. In (c) a phase diagram is constructed from the endothermic peaks observed during first and second heating. Open circles indicate peaks from second heating; solid symbols indicate peaks from first heating. Vertical lines are drawn at stoichiometric ratios between LiTFSI and ethylene oxide (EO) moieties. The symbols C_6, C_3, and C_2 represent stoichiometric ratios of 6, 3, and 2. The symbol L denotes the liquid phase.

semicrystalline samples with $r \leq 0.09$. Figure 5b shows first heating data. Prior to first heating, DSC samples were in the lyophilized state. At salt concentrations $r \geq 0.11$, endothermic peaks were observed upon first heating (but not on second heating) as seen in Figure 5a. We attribute these peaks to slowly crystallizing intermediate compounds formed by PEO and LiTFSI.[29−31] At several salt concentrations, such as $r = 0.35$, two peaks were observed, indicating the coexistence of multiple crystalline phases. Changes in phase coexistence were observed in the vicinity of integer values of $1/r$; at $1/r = 6$, 3, and 2. It is known that PEO/LiTFSI mixtures form crystalline complexes at these salt concentrations. Following the literature, we label these complexes C_6, C_3, and C_2, respectively.[31] Figure 5c shows the phase diagram of the PEO microphases in SEO(16−16)/LiTFSI mixtures, deduced from the DSC peaks observed in the first and second heating. The melting of crystalline solids in electrolytes with $r \leq 0.09$ (open symbols in Figure 5c) were determined from second heating runs. The melting of crystalline solids and their mixtures in electrolytes with $0.15 \leq r \leq 0.55$ (closed symbols in Figure 5c) were determined from first heating runs. The vertical lines in Figure 5c represent locations expected for C_2, C_3, and C_6. The phase diagram in Figure 5c bears close resemblance to the phase diagrams reported by Vallée et al.[30] and Lascaud et al.[31] for homopolymer PEO/LiTFSI. The phase diagram of Lascaud was used to aid in assigning the species in the coexistence regions of Figure 5c; however, separate characterization of the crystal structures is necessary for unambiguous assignment. The PEO-rich microphase of SEO(4.9−5.5) polymers exhibit crystallinity similar to that of SEO(16−16) electrolytes, with corresponding phase transitions occurring at lower temperatures. Data from SEO(4.9−5.5) are included in the Supporting Information (Figure S2).

Ionic conductivity, σ, was measured as a function of salt concentration and temperature for SEO(16−16), SEO(4.9−5.5), and PEO(5). Conductivity as a function of salt concentration and temperature is given in the Supporting Information for each electrolyte in Tables S1−S3. In Figure 6, ionic conductivity at 90 °C is shown for the three polymers. The data at each point in Figure 6 are averaged for three samples, and the error bars represent the standard deviations of the measurements. The ionic conductivity of PEO(5) exhibits a maximum at $r = 0.11$; this value is in reasonable agreement with
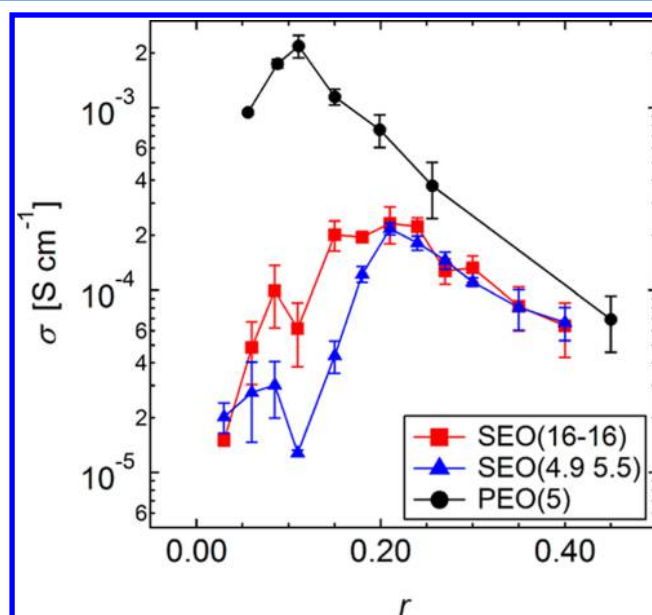

Figure 6. Ionic conductivity, σ, is plotted against salt concentration, r, for the block copolymers SEO(16−16), SEO(4.9−5.5), and homopolymer PEO(5). Data were obtained at 90 °C.

previously reported values for the optimum salt concentration in PEO/LiTFSI mixtures.[30−32] The dependence of conductivity on salt concentration is much richer for SEO(16−16) and SEO(4.9−5.5). Conductivity increases in the range $0 \leq r \leq 0.09$ and decreases in the range $0.09 \leq r \leq 0.11$, before increasing again in the range $0.11 \leq r \leq 0.21$ to obtain a global maximum at $r = 0.21$. Because of the limited range of salt concentrations explored in previous studies on block copolymer electrolytes,[14,15,36] only the local maximum at $r = 0.09$ was captured. Our results show that the trend in conductivity with salt concentration for a homogeneous system such as PEO is qualitatively different than for a nanostructured system such as SEO.

The temperature dependence of ionic conductivity in PEO-based electrolytes has been shown to follow Vogel−Tammann−Fulcher (VTF) behavior.[23] The VTF model for ionic conductivity is given by eq 3:
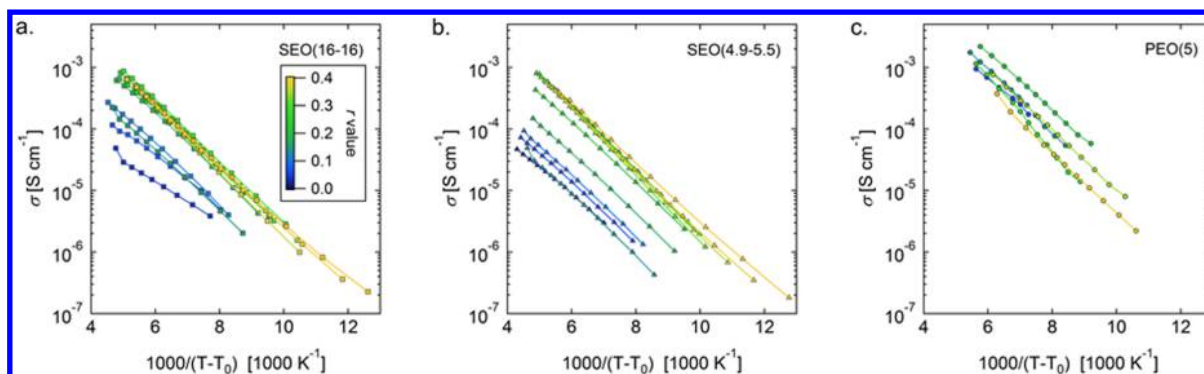
Figure 7. Dependence of conductivity, σ, of SEO(16−16), SEO(4.9−5.5), and PEO(5) on temperature, T, shown on a Vogel−Tammann−Fulcher plot, is presented in (a−c). Each data set represents data at a different salt concentration, and the color scale indicates the r value. The Vogel temperature, T_0, is $T_{g,PEO} - 50$ K, where $T_{g,PEO}$ at the salt concentration of interest is given by the line in Figure 4 and converted to units of kelvin. Data points are connected for clarity.

$$\sigma(T) = A T^{-1/2} e^{-E_a/[R(T-T_0)]} \qquad (3)$$

where A is a prefactor, E_a, is a pseudoactivation energy, R is the gas constant, and T_0 is the Vogel temperature, which is related to the glass transition temperature of the salt-containing microphase ($T_0 = T_{g,PEO} - 50$ °C). The temperature-dependent ionic conductivity data for SEO(16−16), SEO(4.9−5.5), and PEO(5) are shown for different salt concentrations in Figure 7a−c. We restrict our attention to temperatures above $T_{m,PEO}$. These data were fit to the VTF model using A and E_a as adjustable parameters (Figure 8a,b);
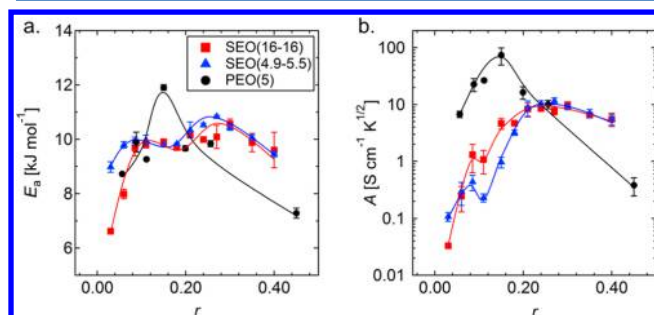

Figure 8. Vogel−Tammann−Fulcher (VTF) parameters for SEO and PEO. The VTF pseudoactivation energy, E_a, and prefactor, A, are plotted against salt concentration, r, in (a) and (b). See eq 3 for definitions of E_a and A. Curves are drawn to guide the eye.

T_0 is determined by the line fit to the $T_{g,PEO}$ data in Figure 4. In Figure 8a, E_a is plotted against r for PEO(5), SEO(16−16), and SEO(4.9−5.5). Values represent the average of E_a calculated for three samples, and error bars show the standard deviation. For PEO(5), E_a exhibits a sharp maximum at $r = 0.11$. For the SEO electrolytes, E_a exhibits two shallow maxima, one near $r = 0.09$ and one near $r = 0.27$, which are close to but not coincident with the maxima in ionic conductivity at 90 °C. In Figure 8b, A is plotted against r for all three types of electrolytes. For PEO(5), A exhibits a sharp maximum at $r = 0.15$. For SEO electrolytes, A exhibits a local maximum at $r = 0.09$ and a shallow global maximum at $r = 0.27$. It is believed that E_a is related to the activation energy associated with ion hopping while A is related to the fraction of dissociated ions (charge carrier concentration).[23] The data in Figure 8 indicate that at high salt concentrations both the activation energy for ion hopping and charge carrier concentration are higher in SEO

electrolytes relative to PEO. These parameters have opposing effects on ionic conductivity. As a result, the conductivities of SEO and PEO electrolytes at high salt concentrations are not significantly different (Figure 6).

The volume fraction of the conducting domains in the SEO electrolytes is a function of salt concentration. To account for this, we compute normalized conductivity, σ_n, defined as

$$\sigma_n = \frac{\sigma_{SEO}(r)}{\phi_c \sigma_{PEO}(r)} \qquad (4)$$

where σ_{SEO} is the ionic conductivity of SEO measured at 90 °C (the data shown in Figure 5a), σ_{PEO} is the ionic conductivity of PEO(5) measured at 90 °C, and ϕ_c is the volume fraction of the combined PEO/LiTFSI domain.[14,47] The volume fraction, ϕ_c, at a given r value was estimated according to eq 5, which assumes that the partial molar volumes of LiTFSI, v_{LiTFSI}, and PEO, v_{PEO}, are unchanged upon mixing.[47]

$$\phi_c = \frac{v_{EO} + r v_{LiTFSI}}{v_{EO} + r v_{LiTFSI} + \frac{n_{PS}}{n_{PEO}} v_S} \qquad (5)$$

In eq 5, n_{PS} is the number of monomers in the PS block and n_{PEO} is the number of the monomers in the PEO block. The number of monomers was calculated from $n = M_{Polymer}/M_{Monomer}$, where M is the molar mass. The molar volume of each species was calculated from $v = M/\rho$, where ρ is the bulk density of the polymer or salt. The molar masses used were 44.05 g mol^{-1} for EO (ethylene oxide monomer), 104.15 g mol^{-1} for S (styrene monomer), and 287.09 g mol^{-1} for LiTFSI. The densities of PEO and PS were calculated to be 1.12 and 1.07 g cm^{-3} at 25 °C from Orwoll,[80] and the density of LiTFSI was taken to be 2.023 g cm^{-3}.[47] The conductivity of PEO used in eq 3, σ_{PEO}, was estimated by linearly interpolating the conductivity data for PEO(5) onto the r values corresponding to the conductivity data for SEO(16−16) and SEO(4.9−5.5).

In Figure 9, we plot σ_n versus r for both SEO(16−16) and SEO(4.9−5.5). The data in Figure 9 are derived from ionic conductivity data obtained at 90 °C (Figure 6). In Figure 9, error is calculated by propagating the error from the PEO and SEO conductivity data in Figure 6. The error from interpolating the values for σ_{PEO} is not accounted for in the figure. Figure 9 shows that both SEO(16−16) and SEO(4.9−5.5) behave similarly with σ_n increasing as a function of r. At concentrations below $r = 0.11$, σ_n of both polymers is around 0.1. Between $r =$
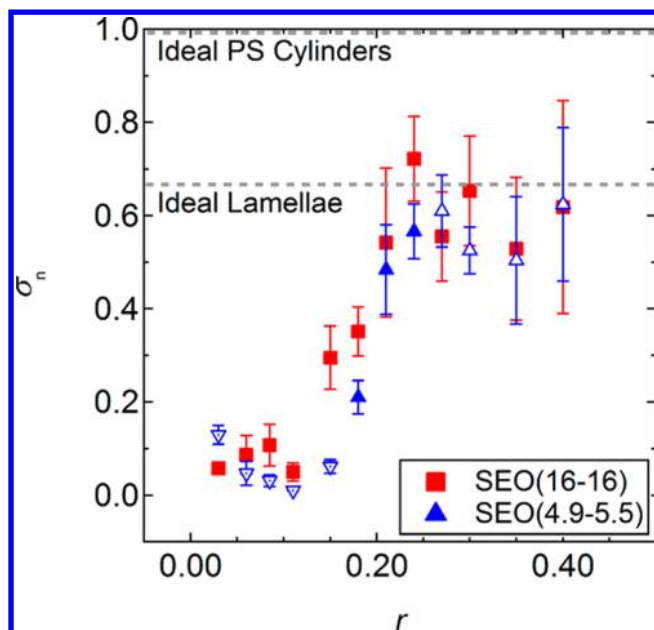
Figure 9. Normalized conductivity, σ_n, is plotted against salt concentration, r. Dashed lines indicate the values of σ_n for ideal lamellae (0.66) and for ideal hexagonally packed PS cylinders in a PEO-rich matrix (1). Open, downward triangles represent compositions of SEO(4.9−5.5)/LiTFSI with entirely lamellar structure, filled, upward triangles indicate lamellae-cylinder coexistence, and open, upward triangles indicate pure cylinder morphologies. Data in Figure 9 are derived from ionic conductivity data taken at 90 °C (Figure 6).

Figure 10. Normalized conductivity, σ_n, is plotted against reduced grain size, L_r, for both SEO(16−16) (squares) and SEO(4.9−5.5) (triangles). The salt concentration, r, is represented by the color of the marker. The curve is an exponential fit through the data. The normalized conductivity is calculated from ionic conductivity data obtained at 90 °C.

0.11 and $r = 0.21$, σ_n increases from 0.1 to about 0.6. At concentrations above $r = 0.21$, σ_n reaches a plateau of about 0.6. For ideal lamellar samples, $\sigma_n = 2/3$, while for ideal cylindrical samples with PEO/LiTFSI in the matrix, $\sigma_n = 1$.[7,15,81] The term ideal implies that our samples are composed of randomly oriented grains with negligible resistance between grains. In other studies, the denominator in eq 5 is scaled by a constant morphology factor.[7,15,81] We omit the morphology factor in eq 5 because for salt concentrations of $0.18 \leq r \leq 0.24$, SEO(4.9−5.5) exhibits coexisting morphologies, and the relative volume fraction of each phase is unclear. Hence, the morphology factor is unknown for several electrolytes in this study. The dashed lines in Figure 9 show the expected values of σ_n for ideal morphologies. It is evident that σ_n of both SEO(16−16) and SEO(4.9−5.5) approaches the expected value for ideal lamellae in the high salt concentration limit. The SAXS and conductivity data (Figures 1a and 9) suggest that ideal lamellar grains are obtained in SEO(16−16) in the high salt concentration limit. On the other hand, the SAXS and conductivity data (Figures 1b and 9) suggest that nonideal cylindrical grains are obtained in SEO(4.9−5.5) in the high salt concentration limit. Previous studies that explored a lower range of salt concentrations ($r \leq 0.1$) reported that σ_n of 2/3 was only reached in lamellar SEO/LiTFSI when the molecular weights of the PS and PEO blocks were each above 60 kg mol^{-1}.[14,15] The present study shows that at sufficient salt loading even low molecular weight SEO polymers can exhibit σ_n values as high as 0.6.

Qualitatively, Figures 2c and 9 are mirror-images of each other, suggesting a relationship between normalized conductivity and reduced grain size. We thus plot σ_n versus L_r of both SEO(16−16) and SEO(4.9−5.5) in Figure 10. The data for SEO(16−16) and SEO(4.9−5.5) collapse on the same trend line. The solid curve in Figure 10 is an exponential fit
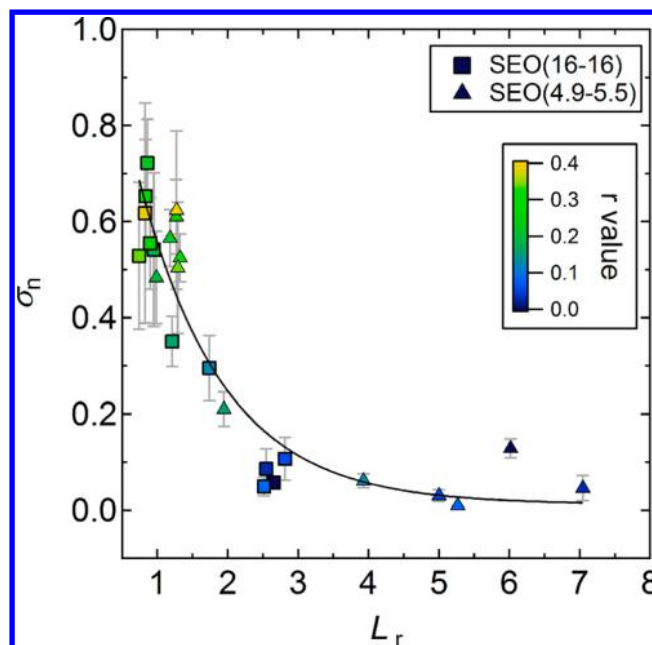
through the data ($\sigma_n = 0.012 + 1.25 \exp[-0.83L_r]$). The error in σ_n in Figure 10 is the same as in Figure 9. The reason for apparent exponential relationship between normalized conductivity and reduced grain size is not known at this time. The correlation between increasing conductivity and decreasing grain size has been demonstrated in a previous study.[17] The reason for this correlation is, however, not well-established. It appears that defects obtained in well-annealed samples with large grains impede the transport of ions, although the particular defects that are responsible for this have not yet been identified. Diederichsen et al. suggest that having smaller grains increases the number of nodes in the conductive path, reducing the importance of any particular node.[82] The result in ref 82 was obtained in thin films of block copolymers, i.e., in two-dimensional samples. Further work is required to establish the underpinnings of the dependence of conductivity on grain size in three-dimensional samples.

The most surprising observation of our study is that in SEO electrolytes ionic conductivity increases in the concentration regime $0.11 \leq r \leq 0.21$, but in PEO(5), ionic conductivity decreases in the same regime. We believe that this is due to the effect of salt concentration on the grain structure in SEO electrolytes.

■ CONCLUSION

The morphology, crystallinity, and ionic conductivity of SEO/LiTFSI electrolytes were determined over a wide range of salt concentrations. The morphology of SEO(16−16) remains lamellar at all salt concentrations studied. The SEO(4.9−5.5) electrolytes undergo morphology transitions from lamellae to coexisting lamellae and majority-PEO cylinders at $r = 0.18$ and from coexistence to cylinders at $r = 0.24$. The crystallinity of the PEO-rich microphase of SEO was found to be similar to that of homopolymer PEO/LiTFSI mixtures, and the glass transition

temperature of the PEO block was similar for both SEO and PEO electrolytes for $r \leq 0.27$. In block copolymer electrolytes that were annealed for a fixed amount of time, the grain size was shown to decrease with increasing salt concentration and then plateau to a value close to the domain spacing of the polymer, indicating a highly defective structure. The effect of salt concentration on grain size of SEO(16−16) and SEO(4.9−5.5) collapses when reduced grain size (grain size normalized by the domain spacing) is plotted as a function of salt concentration.

We show that the dependence of ionic conductivity on salt concentration is qualitatively different for SEO and PEO electrolytes. The maximum in ionic conductivity with salt concentration occurs at about twice the salt concentration in SEO ($r = 0.21$) as in PEO(5) ($r = 0.11$). This result cannot be anticipated from previous systematic studies of conductivity of SEO electrolytes as a functions of salt concentration.[14,15] The electrolytes based on SEO(16−16) and SEO(4.9−5.5) reach similar maximum values of ionic conductivity at 90 °C, 2.3×10^{-4} and 2.2×10^{-4} S cm^{-1}, respectively. For both SEO(16−16) and SEO(4.9−5.5), the normalized conductivity calculated at 90 °C, which takes into account the volume fraction and conductivity of PEO at a given r value, approaches 0.6 in the high salt concentration limit. We show that normalized conductivity decreases exponentially as reduced grain size increases. Increasing salt concentration slows the kinetics of grain growth, which in turn increases block copolymer ionic conductivity.

ASSOCIATED CONTENT

Ⓢ Supporting Information

The Supporting Information is available free of charge on the ACS Publications website at DOI: 10.1021/acs.macromol.5b02620.

> A sample Nyquist impedance plot, the PEO/LiTFSI phase diagram for SEO(4.9−5.5), and raw conductivity data as a function of temperature and salt concentration (PDF)

AUTHOR INFORMATION

Corresponding Author

*E-mail: nbalsara@berkeley.edu (N.P.B.).

Present Address

N.R.V.: Materials Department, University of California, Santa Barbara, Santa Barbara, CA 93106.

Notes

The authors declare no competing financial interest.

ACKNOWLEDGMENTS

ABBREVIATIONS

SEO	polystyrene-*block*-poly(ethylene oxide)
LiTFSI	lithium bis(trifluoromethanesulfonyl)imide
PS	polystyrene
PEO	poly(ethylene oxide)
M_n	number-averaged molecular weight [kg mol^{-1}]
Đ	polymer dispersity
ϕ_{PEO}	volume fraction of the PEO phase in neat SEO
I	scattering intensity [arbitrary]
T_{Sample}	sample transmission
T_{Blank}	blank transmission
σ	ionic conductivity [S cm^{-1}]
t	conductivity sample thickness [cm]
R	electrolyte resistance [Ω]
a	conductivity sample area [cm^2]
T	temperature [K or °C]
T_g	glass transition temperature [°C]
T_m	melting temperature [°C]
q	scattering vector [nm^{-1}]
θ	scattering angle
λ	wavelength [nm]
$q*$	primary peak position [nm^{-1}]
N	number of statistical segments
F	scattering peak full width at half-maximum [nm^{-1}]
d	domain spacing [nm]
L	grain size [nm]
L_r	reduced grain size
χ	Flory−Huggins interaction parameter
A	Vogel−Tammann−Fulcher prefactor [S cm^{-1} K$^{1/2}$]
E_a	Vogel−Tamman−Fulcher activation energy [J mol^{-1}]
T_0	Vogel temperature: $T_g - 50$ °C
σ_n	normalized conductivity
ϕ_c	volume fraction of conductive PEO/LiTFSI phase
v	molar volume [cm^3 mol^{-1}]
n	degree of polymerization
M	molar mass [g mol^{-1}]
ρ	density [g cm^{-3}]

REFERENCES

(1) Tarascon, J. M.; Armand, M. Issues and Challenges Facing Rechargeable Lithium Batteries. *Nature* **2001**, *414* (6861), 359−367.

(2) Goodenough, J. B.; Kim, Y. Challenges for Rechargeable Li Batteries. *Chem. Mater.* **2010**, *22* (3), 587−603.

(3) Monroe, C.; Newman, J. Dendrite Growth in Lithium/Polymer Systems. *J. Electrochem. Soc.* **2003**, *150* (10), A1377.

(4) Zhang, H.; Liu, C.; Zheng, L.; Xu, F.; Feng, W.; Li, H.; Huang, X.; Armand, M.; Nie, J.; Zhou, Z. Lithium Bis(fluorosulfonyl)imide/poly(ethylene Oxide) Polymer Electrolyte. *Electrochim. Acta* **2014**, *133*, 529−538.

(5) Kalhoff, J.; Eshetu, G. G.; Bresser, D.; Passerini, S. Safer Electrolytes for Lithium-Ion Batteries: State of the Art and Perspectives. *ChemSusChem* **2015**, *8* (13), 2154−2175.

(6) Marcinek, M.; Syzdek, J.; Marczewski, M.; Piszcz, M.; Niedzicki, L.; Kalita, M.; Plewa-Marczewska, A.; Bitner, A.; Wieczorek, P.; Trzeciak, T.; et al. Electrolytes for Li-Ion Transport − Review. *Solid State Ionics* **2015**, *276*, 107−126.

(7) Young, W. S.; Kuan, W. F.; Epps, T. H. Block Copolymer Electrolytes for Rechargeable Lithium Batteries. *J. Polym. Sci., Part B: Polym. Phys.* **2014**, *52* (1), 1−16.

(8) Ruzette, A.-V. G.; Soo, P. P.; Sadoway, D. R.; Mayes, A. M. Melt-Formable Block Copolymer Electrolytes for Lithium Rechargeable Batteries. *J. Electrochem. Soc.* **2001**, *148* (6), A537.

(9) Young, W. S.; Epps, T. H. Ionic Conductivities of Block Copolymer Electrolytes with Various Conducting Pathways: Sample Preparation and Processing Considerations. *Macromolecules* **2012**, *45* (11), 4689−4697.

(10) Gu, Y.; Zhang, S.; Martinetti, L.; Lee, K. H.; McIntosh, L. D.; Frisbie, C. D.; Lodge, T. P. High Toughness, High Conductivity Ion Gels by Sequential Triblock Copolymer Self-Assembly and Chemical Cross-Linking. *J. Am. Chem. Soc.* **2013**, *135* (26), 9652−9655.

(11) McIntosh, L. D.; Schulze, M. W.; Irwin, M. T.; Hillmyer, M. A.; Lodge, T. P. Evolution of Morphology, Modulus, and Conductivity in Polymer Electrolytes Prepared via Polymerization-Induced Phase Separation. *Macromolecules* **2015**, *48* (5), 1418−1428.

(12) Bouchet, R.; Phan, T. N. T.; Beaudoin, E.; Devaux, D.; Davidson, P.; Bertin, D.; Denoyel, R. Charge Transport in Nano-structured PS − PEO − PS Triblock Copolymer Electrolytes. *Macromolecules* **2014**, *47* (8), 2659−2665.

(13) Gomez, E. D.; Panday, A.; Feng, E. H.; Chen, V.; Stone, G. M.; Minor, A. M.; Kisielowski, C.; Downing, K. H.; Borodin, O.; Smith, G. D.; et al. Effect of Ion Distribution on Conductivity of Block Copolymer Electrolytes. *Nano Lett.* **2009**, *9* (3), 1212−1216.

(14) Singh, M.; Odusanya, O.; Wilmes, G. M.; Eitouni, H. B.; Gomez, E. D.; Patel, A. J.; Chen, V. L.; Park, M. J.; Fragouli, P.; Iatrou, H.; et al. Effect of Molecular Weight on the Mechanical and Electrical Properties of Block Copolymer Electrolytes. *Macromolecules* **2007**, *40* (13), 4578−4585.

(15) Panday, A.; Mullin, S.; Gomez, E. D.; Wanakule, N.; Chen, V. L.; Hexemer, A.; Pople, J.; Balsara, N. P. Effect of Molecular Weight and Salt Concentration on Conductivity of Block Copolymer Electrolytes. *Macromolecules* **2009**, *42* (13), 4632−4637.

(16) Majewski, P. W.; Gopinadhan, M.; Jang, W.; Lutkenhaus, J. L.; Osuji, C. O. Anisotropic Ionic Conductivity in Block Copolymer Membranes by Magnetic Field Alignment. *J. Am. Chem. Soc.* **2010**, *132* (49), 17516−17522.

(17) Chintapalli, M.; Chen, X. C.; Thelen, J. L.; Teran, A. A.; Wang, X.; Garetz, B. A.; Balsara, N. P. Effect of Grain Size on the Ionic Conductivity of a Block Copolymer Electrolyte. *Macromolecules* **2014**, *47* (15), 5424−5431.

(18) Gunkel, I.; Thurn-Albrecht, T. Thermodynamic and Structural Changes in Ion-Containing Symmetric Diblock Copolymers: A Small-Angle X-Ray Scattering Study. *Macromolecules* **2012**, *45* (1), 283−291.

(19) Zardalidis, G.; Gatsouli, K.; Pispas, S.; Mezger, M.; Floudas, G. Ionic Conductivity, Self-Assembly, and Viscoelasticity in Poly(styrene-B-Ethylene Oxide) Electrolytes Doped with LiTf. *Macromolecules* **2015**, *48*, 7164−7171.

(20) Metwalli, E.; Rasool, M.; Brunner, S.; Müller-Buschbaum, P. Lithium-Salt-Containing High-Molecular-Weight Polystyrene- Block -Polyethylene Oxide Block Copolymer Films. *ChemPhysChem* **2015**, *16*, 2882−2889.

(21) Jo, G.; Ahn, H.; Park, M. J. Simple Route for Tuning the Morphology and Conductivity of Polymer Electrolytes: One End Functional Group Is Enough. *ACS Macro Lett.* **2013**, *2* (11), 990−995.

(22) Ganesan, V.; Pyramitsyn, V.; Bertoni, C.; Shah, M. Mechanisms Underlying Ion Transport in Lamellar Block Copolymer Membranes. *ACS Macro Lett.* **2012**, *1* (4), 513−518.

(23) Armand, M. B.; Chabagno, J. M.; Duclot, M. J. Poly-Ethers as Solid Electrolytes. In *Proceedings of the International Conference on Fast Ion Transport in Solids: Electrodes and Electrolytes*; Vashishta, P., Mundy, J. N., Shenoy, G. K., Eds.; Noth-Holland: New York, 1979; pp 131−136.

(24) Cheng, S.; Smith, D. M.; Li, C. Y. How Does Nanoscale Crystalline Structure Affect Ion Transport in Solid Electrolytes? *Macromolecules* **2014**, *47*, 3978−3986.

(25) Ma, Y.; Doyle, M.; Fuller, T. F.; Doeff, M. M.; De Jonghe, L. C.; Newman, J. The Measurement of a Complete Set of Transport Properties for a Concentrated Solid Polymer Electrolyte Solution. *J. Electrochem. Soc.* **1995**, *142* (6), 1859−1868.

(26) Papke, B. L.; Dupon, R.; Ratner, M. A.; Shriver, D. F. Ion-Pairing in Polyether Solid Electrolytes and Its Influence on Ion Transport. *Solid State Ionics* **1981**, *5*, 685−688.

(27) Robitaille, C. D.; Fauteux, D. Phase Diagrams and Conductivity Characterization of Some PEO-LiX Electrolytes. *J. Electrochem. Soc.* **1986**, *133* (2), 315.

(28) Borodin, O.; Smith, G. D. Mechanism of Ion Transport in Amorphous Poly(ethylene oxide)/LiTFSI from Molecular Dynamics Simulations. *Macromolecules* **2006**, *39* (4), 1620−1629.

(29) Gorecki, W.; Jeannin, M.; Belorizky, E.; Roux, C.; Armand, M. Physical Properties of Solid Polymer Electrolyte PEO(LiTFSI) Complexes. *J. Phys.: Condens. Matter* **1995**, *7* (34), 6823−6832.

(30) Vallée, A.; Besner, S.; Prud'Homme, J. Comparative Study of Poly(ethylene Oxide) Electrolytes Made with LiN(CF3SO2)2, LiCF3SO3 and LiClO4: Thermal Properties and Conductivity Behaviour. *Electrochim. Acta* **1992**, *37* (9), 1579−1583.

(31) Lascaud, S.; Perrier, M.; Vallke, A.; Besner, S.; Prud'homme, J.; Armand, M. Phase Diagrams and Conductivity Behavior of Poly (Ethylene Oxide) -Molten Salt Rubbery Electrolytes. *Macromolecules* **1994**, *27* (25), 7469−7477.

(32) Edman, L.; Ferry, A.; Doeff, M. M. Slow Recrystallization in the Polymer Electrolyte System Poly(ethylene Oxide) n−LiN(CF3SO2)2. *J. Mater. Res.* **2000**, *15* (09), 1950−1954.

(33) Devaux, D.; Bouchet, R.; Glé, D.; Denoyel, R. Mechanism of Ion Transport in PEO/LiTFSI Complexes: Effect of Temperature, Molecular Weight and End Groups. *Solid State Ionics* **2012**, *227*, 119−127.

(34) Rey, I.; Lassègues, J.; Grondin, J.; Servant, L. Infrared and Raman Study of the PEO-LiTFSI Polymer Electrolyte. *Electrochim. Acta* **1998**, *43*, 1505−1510.

(35) Marzantowicz, M.; Krok, F.; Dygas, J. R.; Florjańczyk, Z.; Zygadło-Monikowska, E. The Influence of Phase Segregation on Properties of Semicrystalline PEO:LiTFSI Electrolytes. *Solid State Ionics* **2008**, *179* (27−32), 1670−1678.

(36) Young, W. S.; Epps, T. H. Salt Doping in PEO-Containing Block Copolymers: Counterion and Concentration Effects. *Macromolecules* **2009**, *42* (7), 2672−2678.

(37) Bates, C. M.; Chang, A. B.; Momčilović, N.; Jones, S. C.; Grubbs, R. H. ABA Triblock Brush Polymers: Synthesis, Self-Assembly, Conductivity, and Rheological Properties. *Macromolecules* **2015**, *48* (14), 4967−4973.

(38) Hudson, W. R. *Block Copolymer Electrolytes for Lithium Batteries*; Ph.D. Dissertation, University of California, Berkeley, 2011.

(39) Quirk, R. P.; Kim, J.; Kausch, C.; Chun, M. Butyllithium-Initiated Anionic Synthesis of Well-Defined Poly(styrene-Block-Ethylene Oxide) Block Copolymers with Potassium Salt Additives. *Polym. Int.* **1996**, *39* (1), 3−10.

(40) Hadjichristidis, N.; Iatrou, H.; Pispas, S.; Pitsikalis, M. Anionic Polymerization: High Vacuum Techniques. *J. Polym. Sci., Part A: Polym. Chem.* **2000**, *38* (18), 3211−3234.

(41) Yuan, R.; Teran, A. A.; Gurevitch, I.; Mullin, S. A.; Wanakule, N. S.; Balsara, N. P. Ionic Conductivity of Low Molecular Weight Block Copolymer Electrolytes. *Macromolecules* **2013**, *46* (3), 914−921.

(42) Shi, J.; Vincent, C. The Effect of Molecular Weight on Cation Mobility in Polymer Electrolytes. *Solid State Ionics* **1993**, *60* (1−3), 11−17.

(43) Teran, A. A.; Tang, M. H.; Mullin, S. A.; Balsara, N. P. Effect of Molecular Weight on Conductivity of Polymer Electrolytes. *Solid State Ionics* **2011**, *203* (1), 18−21.

(44) Hexemer, A.; Bras, W.; Glossinger, J.; Schaible, E.; Gann, E.; Kirian, R.; MacDowell, A.; Church, M.; Rude, B.; Padmore, H. A SAXS/WAXS/GISAXS Beamline with Multilayer Monochromator. *J. Phys. Conf. Ser.* **2010**, *247*, 012007.

(45) Ilavsky, J. Nika: Software for Two-Dimensional Data Reduction. *J. Appl. Crystallogr.* **2012**, *45* (2), 324−328.

(46) Allen, F. I.; Ercius, P.; Modestino, M. A.; Segalman, R. A.; Balsara, N. P.; Minor, A. M. Deciphering the Three-Dimensional Morphology of Free-Standing Block Copolymer Thin Films by Transmission Electron Microscopy. *Micron* **2013**, *44*, 442−450.

(47) Teran, A. A.; Balsara, N. P. Thermodynamics of Block Copolymers With and Without Salt. *J. Phys. Chem. B* **2014**, *118* (1), 4−17.

(48) Matsen, M. W.; Bates, F. S. Unifying Weak- and Strong-Segregation Block Copolymer Theories. *Macromolecules* **1996**, *29* (4), 1091−1098.

(49) Bates, F. S.; Fredrickson, G. H. Block Copolymer Thermodynamics: Theory and Experiment. *Annu. Rev. Phys. Chem.* **1990**, *41*, 525−557.

(50) Leibler, L. Theory of Microphase Separation in Block Copolymers. *Macromolecules* **1980**, *13* (6), 1602−1617.

(51) Fredrickson, G. H.; Helfand, E. Fluctuation Effects in the Theory of Microphase Separation in Block Copolymers. *J. Chem. Phys.* **1987**, *87* (1), 697.

(52) Scherrer, P. Estimation of the Size and Structure of Colloidal Particles by Rontgen Rays. *Nachrichten von der K. Gesellschaft der Wissenschaften zu Gottingen, Math. Phys. Klasse* **1918**, No. No.i, 322−323.

(53) Balsara, N. P.; Marques, C. M.; Garetz, B. A.; Newstein, M. C.; Gido, S. P. Anisotropy of Lamellar Block Copolymer Grains. *Phys. Rev. E: Stat. Phys., Plasmas, Fluids, Relat. Interdiscip. Top.* **2002**, *66* (5), 4−7.

(54) Hashimoto, T.; Sakamoto, N.; Koga, T. Nucleation and Growth of Anisotropic Grain in Block Copolymers near Order-Disorder Transition. *Phys. Rev. E: Stat. Phys., Plasmas, Fluids, Relat. Interdiscip. Top.* **1996**, *54* (5), 5832−5835.

(55) Roe, R. J. *Methods of X-Ray and Neutron Scattering in Polymer Science*; Oxford University Press: New York, 2000.

(56) Kim, W. G.; Chang, M. Y.; Garetz, B. A.; Newstein, M. C.; Balsara, N. P.; Lee, J. H.; Hahn, H.; Patel, S. S. Effect of Quench Depth on Grain Structure in Quiescently Ordered Block Copolymers. *J. Chem. Phys.* **2001**, *114* (22), 10196.

(57) Zhang, C. Z.; Wang, Z. G. Random Isotropic Structures and Possible Glass Transitions in Diblock Copolymer Melts. *Phys. Rev. E* **2006**, *73* (3), 1−16.

(58) Dai, H.; Balsara, N.; Garetz, B.; Newstein, M. Grain Growth and Defect Annihilation in Block Copolymers. *Phys. Rev. Lett.* **1996**, *77* (17), 3677−3680.

(59) Ryu, H. J.; Fortner, D. B.; Lee, S.; Ferebee, R.; De Graef, M.; Misichronis, K.; Avgeropoulos, A.; Bockstaller, M. R. Role of Grain Boundary Defects During Grain Coarsening of Lamellar Block Copolymers. *Macromolecules* **2013**, *46* (1), 204−215.

(60) Ryu, H. J.; Fortner, D. B.; Rohrer, G. S.; Bockstaller, M. R. Measuring Relative Grain-Boundary Energies in Block-Copolymer Microstructures. *Phys. Rev. Lett.* **2012**, *108* (10), 107801.

(61) Nishikawa, Y.; Kawada, H.; Hasegawa, H.; Hashimoto, T. Grain Boundary Morphology of Lamellar Microdomains. *Acta Polym.* **1993**, *44* (5), 192−200.

(62) Gido, S. P.; Thomas, E. L. Lamellar Diblock Copolymer Grain Boundary Morphology. 4. Tilt Boundaries. *Macromolecules* **1994**, *27* (21), 6137−6144.

(63) Gido, S. P.; Gunther, J.; Thomas, E. L.; Hoffman, D. Lamellar Diblock Copolymer Grain Boundary Morphology. 1. Twist Boundary Characterization. *Macromolecules* **1993**, *26* (17), 4506−4520.

(64) Jinnai, H.; Yasuda, K.; Nishi, T. Three-Dimensional Observations of Grain Boundary Morphologies in a Cylinder-Forming Block Copolymer. *Macromol. Symp.* **2006**, *245−246* (1), 170−174.

(65) Matsen, M. W. Kink Grain Boundaries in a Block Copolymer Lamellar Phase. *J. Chem. Phys.* **1997**, *107* (19), 8110−8119.

(66) Majewski, P. W.; Yager, K. G. Reordering Transitions during Annealing of Block Copolymer Cylinder Phases. *Soft Matter* **2016**, *12*, 281−294.

(67) Ryu, H. J.; Tong, Q.; Sibener, S. J. Time-Resolved Analysis of Domain Growth and Alignment of Cylinder-Forming Block Copolymers Confined within Nanopatterned Substrates. *J. Phys. Chem. Lett.* **2013**, *4* (17), 2890−2895.

(68) Black, C. T.; Guarini, K. W. Structural Evolution of Cylindrical-Phase Diblock Copolymer Thin Films. *J. Polym. Sci., Part A: Polym. Chem.* **2004**, *42* (8), 1970−1975.

(69) Barrat, J.; Fredrickson, G. H. Diffusion of a Symmetric Block Copolymer in a Periodic Potential. *Macromolecules* **1991**, *24*, 6378−6383.

(70) Lodge, T. P.; Dalvi, M. C. Mechanisms of Chain Diffusion in Lamellar Block Copolymers. *Phys. Rev. Lett.* **1995**, *75* (4), 657−660.

(71) Hamersky, M. W.; Tirrell, M.; Lodge, T. P. Anisotropy of Diffusion in a Lamellar Styrene-Isoprene Block Copolymer. *Langmuir* **1998**, *14* (24), 6974−6979.

(72) Wanakule, N. S.; Virgili, J. M.; Teran, A. A.; Wang, Z.-G.; Balsara, N. P. Thermodynamic Properties of Block Copolymer Electrolytes Containing Imidazolium and Lithium Salts. *Macromolecules* **2010**, *43* (19), 8282−8289.

(73) Wang, J.; Chen, W.; Russell, T. P. Ionic-Complexation-Induced Changes in the Interaction Parameter and the Chain Conformation of PS- B -PMMA Copolymers. *Macromolecules* **2008**, *41* (13), 4904−4907.

(74) Wang, Z.-G. Effects of Ion Solvation on the Miscibility of Binary Polymer Blends. *J. Phys. Chem. B* **2008**, *112* (50), 16205−16213.

(75) Loo, Y. L.; Register, R. A.; Ryan, A. J.; Dee, G. T. Polymer Crystallization Confined in One, Two, or Three Dimensions. *Macromolecules* **2001**, *34* (26), 8968−8977.

(76) Weimann, P. A.; Hajduk, D. A.; Chu, C.; Chaffin, K. A.; Brodil, J. C.; Bates, F. S. Crystallization of Tethered Polyethylene in Confined Geometries. *J. Polym. Sci., Part B: Polym. Phys.* **1999**, *37* (16), 2053−2068.

(77) Zhu, L.; Cheng, S. Z. D.; Calhoun, B. H.; Ge, Q.; Quirk, R. P.; Thomas, E. L.; Hsiao, B. S.; Yeh, F.; Lotz, B. Crystallization Temperature-Dependent Crystal Orientations within Nanoscale Confined Lamellae of a Self-Assembled Crystalline - Amorphous Diblock Copolymer. *J. Am. Chem. Soc.* **2000**, *122* (25), 5957−5967.

(78) Zhu, L.; Cheng, S. Z. D.; Calhoun, B. H.; Ge, Q.; Quirk, R. P.; Thomas, E. L.; Hsiao, B. S.; Yeh, F.; Lotz, B. Phase Structures and Morphologies Determined by Self-Organization, Vitrification, and Crystallization: Confined Crystallization in an Ordered Lamellar Phase of PEO-B-PS Diblock Copolymer. *Polymer* **2001**, *42* (13), 5829−5839.

(79) Huang, P.; Zhu, L.; Cheng, S. Z. D.; Ge, Q.; Quirk, R. P.; Thomas, E. L.; Lotz, B.; Hsiao, B. S.; Liu, L.; Yeh, F. Crystal Orientation Changes in Two-Dimensionally Confined Nanocylinders in a Poly (Ethylene Oxide) - B -Polystyrene/Polystyrene Blend. *Macromolecules* **2001**, *34* (19), 6649−6657.

(80) Orwoll, R. A. In *Physical Properties of Polymers Handbook*; Mark, J. E., Ed.; Springer: New York, 2007; pp 94−95.

(81) Sax, J.; Ottino, J. M. Modeling of Transport of Small Molecules in Polymer Blends: Application of Effective Medium Theory. *Polym. Eng. Sci.* **1983**, *23* (3), 165−176.

(82) Diederichsen, K. M.; Brow, R. R.; Stoykovich, M. P. Percolating Transport and the Conductive Scaling Relationship in Lamellar Block Copolymers under Confinement. *ACS Nano* **2015**, *9* (3), 2465−2476.